ACS APPLIED MATERIALS & INTERFACES

Research Article

www.acsami.org

Composition-Controlled PtCo Alloy Nanocubes with Tuned Electrocatalytic Activity for Oxygen Reduction

Sang-Il Choi,† Su-Un Lee,† Woo Youn Kim,* Ran Choi, Kwangwoo Hong, Ki Min Nam, Sang Woo Han,* and Joon T. Park*

Department of Chemistry, KAIST, Daejeon 305-701, Korea

Supporting Information

ABSTRACT: Modification of the electronic structure and lattice contraction of Pt alloy nanocatalysts through control over their morphology and composition has been a crucial issue for improving their electrocatalytic oxygen reduction reaction (ORR) activity. In the present work, we synthesized PtCo alloy nanocubes with controlled compositions (Pt_xCo NCs, x = 2, 3, 5, 7, and 9) by regulating the ratio of surfactants and the amount of Co precursor to elucidate the effect of the composition of nanocatalysts on their ORR activity. Pt_xCo NCs had a Pt-skin structure after electrochemical treatment. The electrocatalysis experiments revealed a strong correlation between ORR activity and Co composition. Pt_3Co NCs exhibited the best ORR performance among the various Pt_xCo NCs. From density functional theory calculations, a typical volcano-type relationship was established between ORR activity and oxygen binding energy (E_{OB}) on NC surfaces, which showed that Pt_3Co NCs had the optimal E_{OB} to achieve the maximum ORR activity. X-ray photoelectron spectroscopy and X-ray diffraction measurements demonstrated that the electronic structure and lattice contraction of the Pt_xCo NCs could be tuned by controlling the composition of NCs, which are highly correlated with the trends of E_{OB} change.

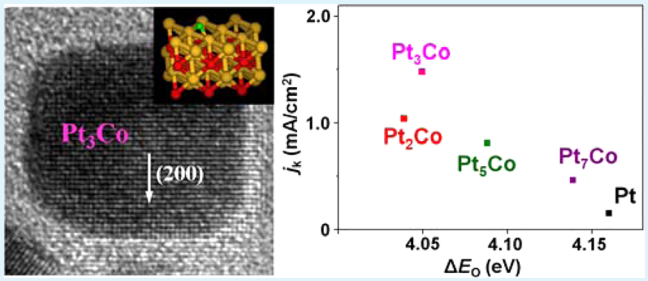

KEYWORDS: *cobalt, fuel cells, nanocubes, oxygen reduction, platinum*

INTRODUCTION

One of the main challenges for developing the performance of low-temperature fuel cells and metal−air batteries is improving the activity of cathodic catalysts toward oxygen reduction reaction (ORR).[1−7] Expensive Pt-based catalysts, such as supported Pt/C catalysts, have been used as electrocatalysts in the cathode for the ORR.[8−11] Recent studies have aimed to enhance the activity of Pt-based catalysts toward oxygen reduction to reduce the Pt requirement and thus to minimize cost.[3,4,8,9,12−35] In particular, there have been intensive studies on Pt-transition metal (Fe, Co, Ni, etc.) alloy nanocatalysts because they have shown improved ORR activities in comparison to pure Pt catalysts, which originate from the modified electronic structures of Pt induced by the incorporation of other foreign metals (ligand effect).[3,4,12−25] Stamenkovic et al. demonstrated that alloying Pt with 3d transition metals tunes its electronic structure, and consequently, changes its performance toward the ORR.[22] ORR activity highly depends on the position of the metal d-band center relative to the Fermi level, and it is in good agreement with the oxygen−metal bond interaction model. Recently, it has also been reported that the ORR performance of Pt-based bimetallic nanoparticles can be modulated by the amount of lattice contraction (geometric effect).[26,36] A surface Pt layer with moderate lattice contraction induces the enhancement of the ORR activity.[26]

Controlling the morphology/shape and composition of Pt-3d transition metal alloy nanocatalysts is of primary importance in the fine-tuning of electronic and surface geometric structures, and in turn, in improving their ORR efficiencies.[13−17,26−35] For instance, Zhang et al. reported the synthesis of the octahedral and cubic shapes of Pt_3Ni nanocrystals with highly enhanced activities for the ORR, which demonstrates that the morphology control of Pt-transition metal alloy nanocatalysts should be a promising approach to improve their electrocatalytic activity.[16] In a previous work, we have shown that Pt_3Co nanocubes have higher ORR activity than that of truncated octahedral Pt_3Co nanocrystals in H_2SO_4 media.[14] On the other hand, in a study on dealloyed Pt−Cu catalysts with various Cu contents prepared by an annealing process in high temperature, Strasser and co-workers reported that the $PtCu_3$ catalyst exhibited the maximum ORR activity among the prepared catalysts.[26] In addition, composition-controlled Pt−Ni nanoparticles, supported on carbon, exhibited a volcano type relationship between the ORR activity and metal composition, where Pt_2Ni catalyst showed the best performance toward the ORR.[24]

Received: August 29, 2012
Accepted: October 29, 2012
Published: October 29, 2012

Other recent studies have reported encouraging observations for Pt-transition metal alloy nanocatalysts. As in the case of extended surfaces of bimetallic alloy thin films, the formation of Pt-skin surfaces through the thermal annealing process profoundly enhanced the ORR catalytic activity of Pt–transition metal alloy nanoparticles.[19] The annealing process induced the surface segregation of the topmost atomic layer of Pt alloys, resulting in the formation of Pt-enriched surfaces. The Pt-skin of Pt alloy nanocatalysts, which is stable in the electrochemical environment, acts as a protecting layer for the underneath alloy layers. A recent scanning transmission electron microscopy (STEM) study revealed that a Pt-skin protecting Pt alloy nanoparticles also formed in electrochemical potential cycling.[25] Because the electronic and geometric structures of surface Pt atoms in the Pt-skin structures can be more effectively modulated in comparison to mixed-skin structures, it can be expected that ORR catalysts with superior activities can be developed from these structures through the optimization of interactions between Pt atoms and oxygenated species of the ORR. Nevertheless, trend in ORR activity and its correlation with the electronic structure/geometric contraction for such structures along the variations of composition and morphology has not been thoroughly explored.

We report here on the synthesis of Pt(100) facet-exposed Pt-skin Pt_xCo (x = 2, 3, 5, 7, and 9) nanocubes (NCs) and their composition-dependent ORR performance. The Pt-skin structure of Pt_xCo NCs was obtained by electrochemical treatment. The electronic structure and geometric surface contraction of Pt_xCo NCs were tuned by changing the composition of the NCs, as shown by X-ray photoelectron spectroscopy (XPS) and X-ray diffraction (XRD), resulting in the modulation of their ORR activities. Among the various Pt_xCo NC catalysts, Pt_3Co NCs exhibited significantly improved ORR activity, showing that the cubic shape with an appropriate Co content is the key to obtaining high ORR activity. To understand the correlation between the oxygen binding energy (E_{OB}) on Pt(100) surfaces and the ORR activity, we have performed density functional theory (DFT) calculations by adopting a Pt-skin slab model of the Pt_xCo NCs. This model has shown a typical volcano-shaped plot, implying that the experimentally obtained ORR activities are highly correlated with the E_{OB} which is regulated by the compositions of the Pt_xCo NCs.

EXPERIMENTAL SECTION

Materials. Platinum(II) acetylacetonate ($Pt(acac)_2$), 1,2-hexadecanediol, oleylamine (OAm, >70%), oleic acid (OA, 90%), and benzyl ether (99%) were purchased from Aldrich and used without further purification. Dicobalt octacarbonyl ($Co_2(CO)_8$) was purchased from Strem chemicals.

Synthesis of 8 nm Pt_xCo (x = 2, 3, 5, 7, and 9) NCs. To a mixture of $Pt(acac)_2$ (25 mg, 0.064 mmol) and $Co_2(CO)_8$ (5.4 mg, 0.016 mmol for x = 3, 5, 7, and 9; 8.1 mg, 0.024 mmol for x = 2) in a 250 mL flask were added 1,2-hexadecanediol (15 mg), benzyl ether (4 mL), OAm (4 mL for x = 2 and 3, 2 mL for x = 5, 1 mL for x = 7, and 0.5 mL for x = 9), and OA (0.5 mL) in a drybox. The slurry was heated from 120 to 200 °C for 30 min with a heating rate of 2–3 °C min^{-1} and kept at 200 °C for 90 min under an argon atmosphere to give a black-brown suspension. The resulting reaction mixture was diluted with toluene (10 mL), and Pt_xCo NCs were precipitated by adding ethanol (25 mL). The supernatant was removed by centrifugation at 3000 rpm for 10 min. The resulting Pt_xCo NCs were easily dispersed in organic solvents such as toluene and hexane.

Preparation of Pt_xCo/C catalysts. Each solution of Pt_xCo NCs was added to 29.1 mg of Ketjen Black (KB) carbon (30 wt % Pt) dispersed in toluene under ultrasonic wave agitation for 10 min. The mixtures were stirred and ultrasonicated for 5 h. The resulting Pt_xCo NCs deposited on a carbon support (Pt_xCo/C) were ultrasonicated in toluene for 10 min to remove the stabilizers, and then the supernatant was removed by centrifugation at 10,000 rpm for 15 min. This washing and centrifuging steps were conducted repeatedly for 5 times. Then the Pt_xCo/C catalysts were ultrasonicated in ethanol for 10 min to facilitate their easy dispersion in water, and the supernatant was removed by centrifugation at 10,000 rpm for 15 min. All the catalysts were vacuum-dried for 30 min before use.

Characterization of NCs. Transmission electron microscopy (TEM) images were obtained with an Omega EM912 transmission electron microscope operating at 120 kV and Philips CM20 transmission electron microscope operating at 160 kV. High-resolution TEM (HRTEM), fast Fourier-transform (FFT) patterns, and energy-dispersive X-ray spectroscopy (EDS) characterizations were performed with a Philips F20 Tecnai transmission electron microscope operating at 200 kV and FEI Tecnai G2 F30 transmission electron microscope operating at 300 kV. Compositional line profile analyses and STEM-EDS mapping were performed by using a JEOL JEM-ARM200F spherical aberration corrected (Cs-corrected) STEM operating at 200 kV. The compositions of Pt_xCo NCs were determined by EDS, inductively coupled plasma-atomic emission spectroscopy (ICP-AES, Perkin-Elmer OPTIMA 7300 DV), and XPS. XPS measurements were carried out using a Thermo MultiLab 2000 spectrometer with Al Kα X-ray (1486.6 eV) as the light source. XRD patterns were obtained with a Rigaku D/MAX-RB diffractometer using Cu Kα (0.1542 nm) radiation.

Electrochemical Measurements. Electrochemical studies were carried out at room temperature in a three-electrode cell using a CHI 760D potentiostat (CH Instrument). Pt wire and Ag/AgCl (in saturated NaCl) were used as the counter and reference electrodes, respectively. All the potentials were reported with respect to the reversible hydrogen electrode (RHE). To prepare working electrode, 5 μL of the catalyst dispersion, which was prepared by mixing 2 mg of the carbon-supported catalysts with a mixed solution of 50 μL of diluted Nafion alcohol solution (Fluka, 5.0 wt %) and 1 mL of deionized water, was dropped onto a glassy carbon electrode (GCE) and carefully dried it in an oven at 90 °C for 5 min. For cyclic voltammetry (CV) measurements, the electrode potential was cycled between 0.08 and 1.28 V with a scan rate of 20 mV s^{-1} in 0.5 M H_2SO_4 aqueous solution purged with N_2 for 30 min before use. The catalysts were activated by 30 potential cycles under identical conditions. Rotating disk electrode (RDE) experiments were carried out using a rotator (BAS, RDE-2) in 0.5 M H_2SO_4 aqueous solution purged with O_2 prior to use for 30 min. The following Koutecky–Levich (KL) equation estimated the kinetic current densities (j_k)

$$1/j = 1/j_k + 1/j_d = 1/j_k + 1/B\omega^{1/2} \quad (1)$$

where j_d is the diffusion-limited current density and ω is the angular frequency of rotation. The B parameter is defined by the following equation

$$B = 0.62nFC_oD_o^{2/3}\upsilon^{-1/6} \quad (2)$$

where n is the overall number of electrons, F is the Faraday constant (96,485 C mol^{-1}), C_0 is the concentration of molecular oxygen in the electrolyte (1.26×10^{-6} mol cm^{-3}), D_0 is the diffusion coefficient of the molecular O_2 in 0.5 M H_2SO_4 solution (1.93×10^{-5} cm^2 s^{-1}), and υ is the viscosity of the electrolyte (1.009×10^{-2} cm^2 s^{-1}). Electrochemically active surface areas (ECSA) of catalysts were calculated by integrating the charges in the underpotential hydrogen adsorption/desorption (H_{UPD}) region of the CV curves.[13,37,38]

Preparation of XPS Samples. Half a milligram of KB carbon-supported catalysts dispersed in ethanol (0.25 mL) was dropped onto an Au film and the solvent was slowly evaporated. For electrochemical treatment of each sample, 20 times of linear potential sweep between −0.08 to 1.28 V were performed with a scan rate of 50 mV s^{-1} in a N_2-saturated 0.5 M H_2SO_4 solution at room temperature.

Computational Methods. The binding energy of an oxygen atom (E_{OB}) on the surface of Pt_xCo (x = 2, 3, 5, and 7) NCs has been calculated using the VASP package[39−42] based on the DFT with the Perdew-Burke-Ernzerhof exchange-correlation functional.[43] We chose the (100)-faceted faced-centered cubic (*fcc*) crystal structure to model the NC surfaces. The lattice constants of the Pt_xCo NCs were obtained from the XRD measurement; 3.900, 3.906, 3.912, and 3.914 Å for x = 2, 3, 5, and 7, respectively. To mimic the surface structure, a slab model with (3 × 2) unit cells including 4-metal layers was employed. The two top layers were fully relaxed, while the others were frozen. The distance between slabs was about 16 Å, equivalent to eight metal layers. We have checked that the energy cutoff of 400 eV and 3 × 5 k-points were sufficient to yield reliable binding energies. To seek out plausible surface structures for a given composition of each NC, we compared total energies of various configurations in the bulk phase, and concluded that the more uniform the configuration, the more stable the structure. To calculate binding energies, we considered two different surface conditions; one had the same composition as its bulk, but the other had a 100% Pt top layer, namely mixed-skin and Pt-skin models, respectively (Figure 1). For both cases, the most stable

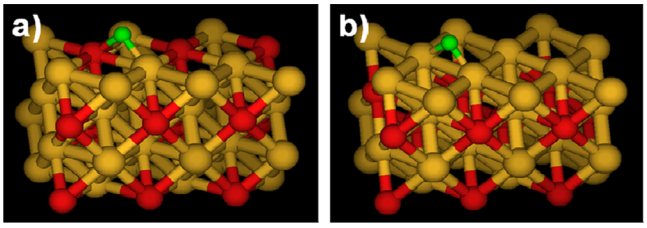

Figure 1. Slab models of (100) facet-exposed Pt_3Co NCs with an adsorbed O atom for (a) mixed-skin and (b) Pt-skin structure (yellow, Pt; red, Co; green, O atom).

binding position of an oxygen atom turned out to be the bridge site of the (100) facet, whereas the (111) facet favored the hollow site.[44,45] This can be due to the fact that the (100) facet has a larger interatomic distance than that of the (111) facet. The oxygen atom favored the bridge site between Pt and Co atoms in the case of the mixed-skin model, but bound too strongly as compared to pure Pt, which may have led to decreased ORR activity.[22] Therefore, we chose the less stable Pt-skin model for DFT calculations. In fact, the Pt_xCo NCs had the Pt-skin structure after electrochemical treatment. The E_{OB} values were calculated from the following equation

$$E_{OB} = E_{total} - E_{substrate} - E_{gas\text{-}phase\ adsorbate} \quad (3)$$

where E_{total} is the total energy of the Pt_xCo slab with an O atom, $E_{substrate}$ is the energy of the slab, and $E_{gas\text{-}phase\ adsorbate}$ is the energy of the free O atom in the gas phase.

RESULTS AND DISCUSSION

The Pt_xCo NCs were synthesized by using a cosurfactant system consisting of OAm and OA.[13,37] The OAm/OA ratio in the initial mixture substantially influenced the composition of the resultant Pt_xCo NCs. In previous works, we found that Pt_9Co NCs were prepared with a 1:1 molar ratio of OAm/OA and that an 8-fold increase of the relative amount of OAm produced Pt_3Co nanocrystals.[13,14] The easy coordination of Co to OA hindered the full decomposition of $Co_2(CO)_8$; the relative content of Co increases as the relative amount of OA decreases.[46] Based on this finding, we diversified the OAm/OA ratio to prepare Pt_xCo NCs with various Pt/Co ratios. OAm/OA ratios of 1, 2, 4, and 8 led to the formation of Pt_9Co, Pt_7Co, Pt_5Co, and Pt_3Co NCs, respectively. Increasing the amount of Co precursor by 1.5 times with the OAm/OA ratio of 8 produced the Pt_2Co NCs. Table 1 summarizes the atomic compositions of the prepared Pt_xCo NCs determined by EDS, ICP-AES, and XPS.

Table 1. Pt/Co Molar Ratios of the Pt_xCo NCs Obtained by EDS, ICP-AES, and XPS

	Pt_9Co	Pt_7Co	Pt_5Co	Pt_3Co	Pt_2Co
EDS	6.8:1	6.2:1	4.3:1	2.9:1	2.5:1
ICP-AES	8.5:1	5.6:1	4.8:1	3.1:1	1.9:1
XPS	8.6:1	6.8:1	4.4:1	2.8:1	2.3:1

Figure 2a, d, g, j, and m show typical TEM images of the as-synthesized Pt_xCo NCs, revealing that homogeneous Pt_xCo NCs with an average edge length of 8 nm were yielded regardless of the compositions of NCs. A low-magnification TEM image of the Pt_3Co NCs further demonstrates the high uniformity of NCs in shape and size (Figure S1 in the Supporting Information). Figure 2b, e, h, k, and n show HRTEM images of individual Pt_xCo NCs with different compositions, indicating the highly crystalline structure of NCs. The *d*-spacing between the adjacent lattice fringes of Pt_9Co NC was measured to be 1.96 Å, which was identical to that of the (200) planes of fcc Pt crystal (Figure 2b). The fast Fourier transform (FFT) patterns of the Pt_xCo NCs shown in Figure 2c, f, i, l, and o further imply that the Pt_xCo NCs are single crystals enclosed by {100} facets.

To get more insight into the crystal structure of the Pt_xCo NCs, the XRD patterns of the samples were obtained (Figure 3). The diffraction patterns of the Pt_xCo NCs (the upper traces of each labeled set in Figure 3) reveal that they have highly crystalline natures. All the diffraction peaks are well-correlated with those of the standard fcc Pt (JCPDS, card no. 04−0802). Slow evaporation of the toluene dispersion of NCs on glass substrates could fabricate well-ordered assemblies of the Pt_xCo NCs. The overwhelmingly enhanced (200) peak and the absence of other diffraction peaks in each XRD pattern of the assembled NCs (the lower traces of each labeled set in Figure 3) show that the Pt_xCo NCs are enclosed predominantly by {100} facets as revealed by TEM measurements. The crystallite sizes of the NCs were determined to be 7.3, 8.0, 7.1, 7.2, and 7.3 nm for Pt_9Co, Pt_7Co, Pt_5Co, Pt_3Co, and Pt_2Co NCs, respectively, by using the Debye−Scherrer equation. These values were closely matched with the average size of NCs obtained from TEM images, indicating that the as-synthesized Pt_xCo NCs were single-crystalline nanocrystals.[47] When compared to the standard Pt, the diffraction peaks were gradually shifted to higher 2θ values as the Co composition of Pt_xCo NCs increased ((200) peaks were observed at 46.17, 46.49, 46.59, 46.77, and 47.00° for Pt_9Co, Pt_7Co, Pt_5Co, Pt_3Co, and Pt_2Co NCs, respectively), which could be attributed to the decrease of lattice distance along the increase of the amount of smaller Co atoms (1.26 Å) in place of Pt atoms (1.36 Å).[48] As mentioned previously, the lattice contraction enhances the ORR activity of Pt-based nanocatalysts by reducing the binding energy of oxygenated adsorbates, such as O and OH, on their surfaces, which results in activating the proton and electron transfer rates of catalytically active surface sites.[26] However, there exists a critical point for the lattice contraction, beyond which the ORR activity reduces due to the formation of OOH intermediate.[49] On the basis of this fact and experimental observations, it can be expected that there would be a certain correlation between the lattice distance of the Pt_xCo NCs and

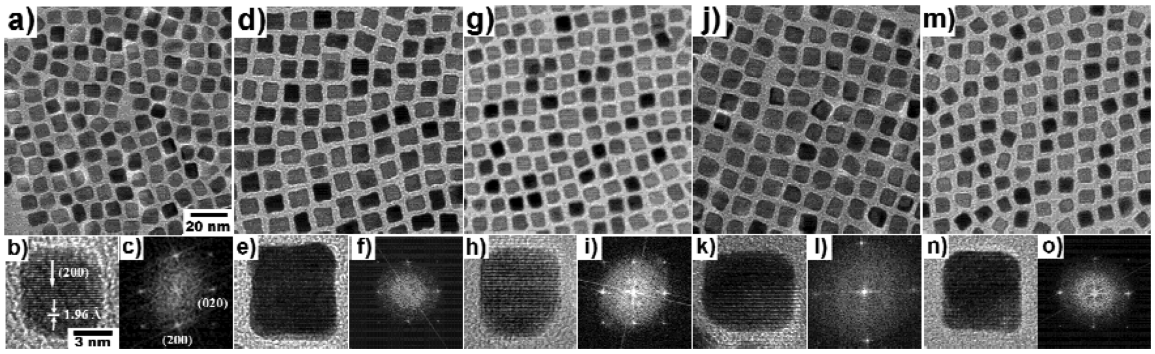

Figure 2. (a, d, g, j, m) TEM images, (b, e, h, k, n) HRTEM images, and (c, f, i, l, o) corresponding FFT patterns of (a–c) Pt_9Co, (d–f) Pt_7Co, (g–i) Pt_5Co, (j–l) Pt_3Co, and (m–o) Pt_2Co NCs.

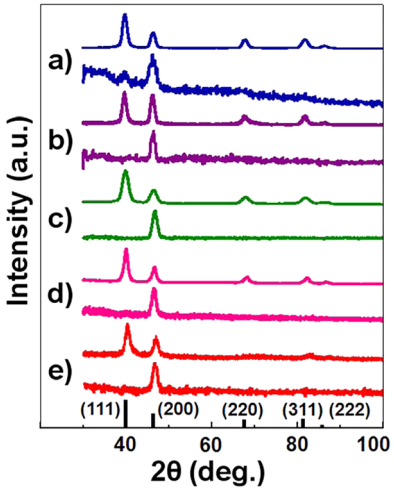

Figure 3. XRD patterns of (a) Pt_9Co, (b) Pt_7Co, (c) Pt_5Co, (d) Pt_3Co, and (e) Pt_2Co NCs. The lower traces of each labeled set are the XRD patterns of self-assembled Pt_xCo NCs. The intensity and position for Pt reference (black lines at the bottom) were taken from the JCPDS database.

their catalytic activity toward the ORR. This will be discussed later (vide infra).

The ORR activities of Pt_xCo NCs supported on KB carbon (Pt_xCo/C, 30 wt %, see Figure S2 in the Supporting Information) were investigated. For comparison, carbon-supported monometallic Pt NC (average edge length = 8 nm) catalysts were also prepared (Pt_c/C, 30 wt %, see Figure S3 in the Supporting Information). Figure 4a shows the CV data of Pt_xCo/C and Pt_c/C catalysts in N_2-saturated 0.5 M H_2SO_4 at room temperature. In the H_{UPD} region (from 0.08 to 0.4 V), characteristic peaks for the Pt(100) were observed at about 0.25 V.[13] This was in good agreement with the results of TEM and XRD analyses.

The ORR activities for catalysts were measured with a RDE at a rotation rate of 1600 rpm and a sweep rate of 20 mV s^{-1} in O_2-saturated 0.5 M H_2SO_4 (Figure 4b). The specific kinetic current densities (j_k in mA cm^{-2}) normalized to the geometric area of the RDE (0.07065 cm^2), were obtained by the KL equation (eq 1). Figure 4c shows the KL plots (j^{-1} vs $\omega^{-1/2}$) at 0.9 V for the Pt_xCo/C and Pt_c/C catalysts. Figure 4d shows the j_k values of the catalysts as a function of potential, calculated with the KL equation. At 0.9 V, the current densities for the catalysts were 0.14 (Pt_c/C), 0.37 (Pt_9Co/C), 0.46 (Pt_7Co/C), 0.81 (Pt_5Co/C), 1.48 (Pt_3Co/C), and 1.04 (Pt_2Co/C) mA cm^{-2} (Figure 4e). The mass activities, normalized to the Pt mass of the nanocatalysts, were 0.037 (Pt_c/C), 0.103 (Pt_9Co/C), 0.129 (Pt_7Co/C), 0.229 (Pt_5Co/C), 0.434 (Pt_3Co/C), and 0.322 (Pt_2Co/C) A mg_{Pt}^{-1} (Figure 4e). As shown in Figure 4e, the Pt_xCo/C catalysts had higher ORR activities than that of the Pt_c/C catalysts and the Pt_3Co/C exhibited the highest current density and mass activity for the ORR among the various catalysts.

The reason of the superior ORR specific and mass activity of the Pt_3Co/C to other catalysts can be explained by the ORR kinetic model proposed by Stamenkovic and co-workers.[22] Electrocatalytic activity strongly depends on the E_{OB} on a catalytic surface. Too strong binding energy provokes permanent surface oxidation and thus degrades its activity, while too weak binding energy readily causes desorption of oxygen from the active site before reduction. As a result, the maximum ORR activity occurs with a catalyst surface that has an appropriate E_{OB}, balancing the surface oxidation and disgregation simultaneously, which is characterized by the well-known volcano-shape dependence of the ORR activity on the E_{OB}.[19,22] Accordingly, we can expect that the Pt_3Co NCs might have an optimum E_{OB} for the ORR. To verify the correlation between the E_{OB} and the ORR activity, we have calculated the E_{OB} of the Pt NC and Pt_xCo NCs using the Pt-skin slab model (Figure 1b). Although as-synthesized Pt_xCo NCs showed a mixed-skin surface consisting of both Pt and Co atoms, the Pt-skin type structures of Pt_xCo NCs were obtained after electrochemical treatment as a result of dealloying.[25] This can be evidenced by the compositional line profile and elemental mapping analyses for the NCs with Cs-corrected STEM (Figure S4 in the Supporting Information). HRTEM measurements also revealed the formation of the Pt-skin Pt_xCo NCs (Figure S5 in the Supporting Information). In addition, the Co compositions in Pt_xCo determined by XPS were decreased after the electrochemical treatment (Table S1 in the Supporting Information), implying that the dissolution of Co during the treatment resulted in the formation of Pt-skin structures. Comparison of CV curves of carbon-supported NCs obtained before and after the electrochemical treatment further identified the dealloying process: the appearance of distinct peaks for the Pt(100) surface in the H_{UPD} region, the narrowing of the double-layer charging current, and the positive shift of Pt oxidation potential were observed in the CV curve after the electrochemical treatment (Figure S6 in the Supporting Information).[50] As shown in Figure 5, the DFT-calculated E_{OB} of the NC decreased as the Co content in the NC increased. This agreed well with the experimental results

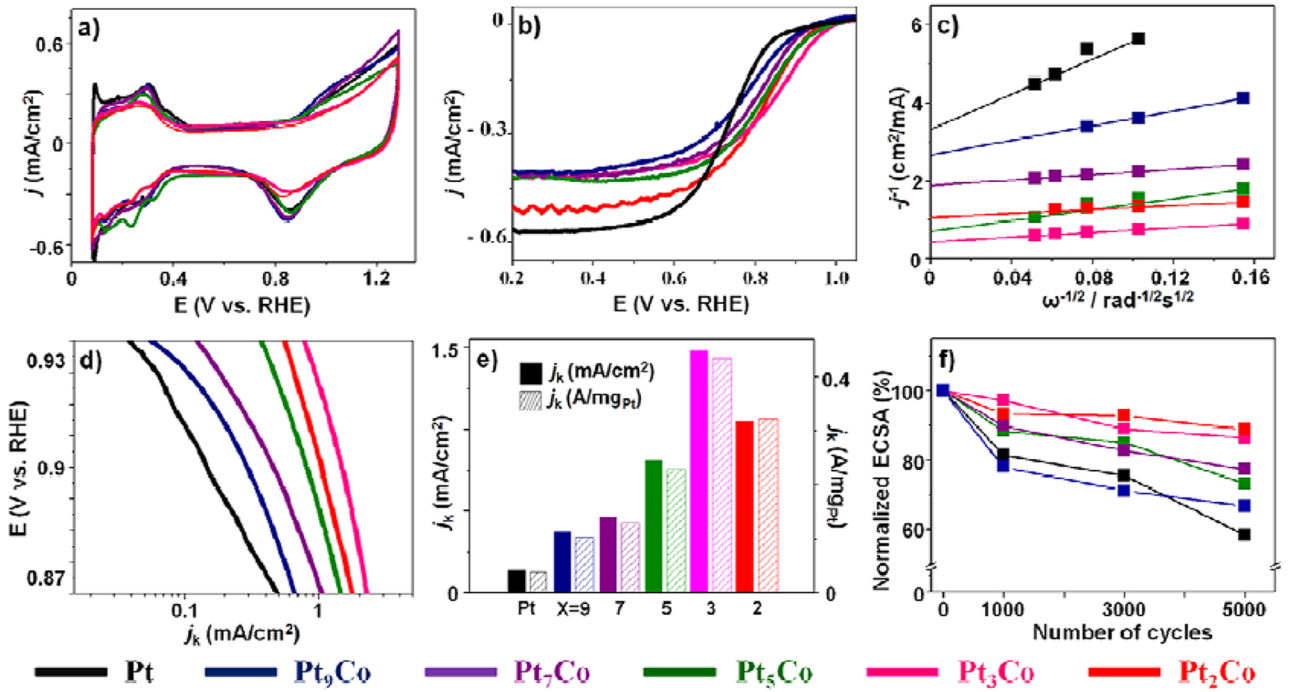

Figure 4. (a) CV curves of the Pt_xCo/C and Pt_c/C obtained in 0.5 M H_2SO_4 at a scan rate of 20 mV s^{-1}. (b) The polarization curves in O_2-saturated 0.5 M H_2SO_4 at a scan rate of 20 mV s^{-1} and a rotation rate of 1600 rpm. (c) KL plots for oxygen reduction with the various catalysts at 0.9 V vs RHE. (d) The j_k values as a function potential for the various catalysts. (e) Specific kinetic current densities and mass activities at 0.9 V vs RHE for the Pt_xCo/C and Pt_c/C catalysts. (f) The normalized ECSA for the various catalysts as a function of the number of cycles in accelerated durability tests.

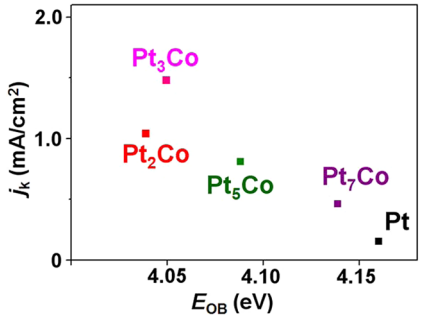

Figure 5. ORR activity versus the DFT-calculated E_{OB} of Pt-skin Pt_xCo NCs and Pt NC.

obtained in the CV measurements: the oxidation peak for the formation of the adsorbed hydroxyl (OH_{ad}) species above 0.8 V shifted more positively as the composition of Co in the Pt_xCo NCs increased (Figure 4a).[12] Furthermore, the plot of the experimental ORR activities as a function of the E_{OB} manifested the typical volcano-shape trend, where the Pt_3Co NC located at the peak. Consequently, as mentioned above, the Pt_3Co NC had the optimal E_{OB} to achieve the maximum ORR activity among the various catalysts.

The E_{OB} on a catalyst surface, a good descriptor for the ORR activity, is highly correlated with the relative position of the metal d-band center to the Fermi level of the catalyst.[22] The E_{OB} on Pt-3d transition metal alloy nanocatalysts can be lower than that of pure Pt when the position of their d-band center is downward shifted relative to that of Pt, because the antibonding orbitals of the Pt−O bond are more populated along the downshift of the d-band center.[22] To investigate the modification of the electronic structure of the Pt_xCo NCs, we performed XPS measurements on the Pt-skin Pt_xCo/C and Pt_c/C catalysts. XPS spectra for the Pt 4f core level of Pt_xCo/C and Pt_c/C are shown in Figure 6. Core level XPS measurement

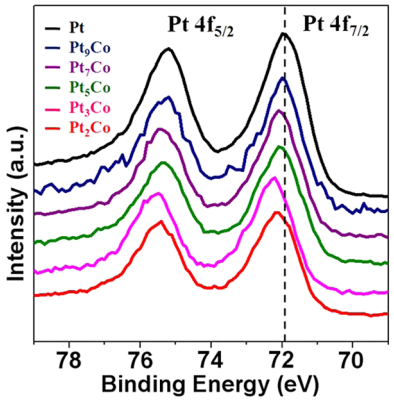

Figure 6. XPS spectra for the Pt 4f core-level of Pt_c/C and Pt-skin Pt_xCo/C prepared by the electrochemical treatment.

has been widely used to evaluate d-band shifts due to its high correlation with valence band XPS.[51] Noticeably, the Pt 4f binding energies of the Pt_xCo/C were blue-shifted compared to the Pt_c/C; the positions of Pt $4f_{7/2}$ peaks were 71.96, 72.01, 72.08, 72.07, 72.23, and 72.17 eV for Pt_c/C, Pt_9Co/C, Pt_7Co/C, Pt_5Co/C, Pt_3Co/C, and Pt_2Co/C, respectively. This indicates that the d-band centers of the Pt_xCo/C catalysts downshifted compared to that of the Pt_c/C, and the trend of the d-band shift was strongly correlated with that of the E_{OB}. Previous works on Pt−Co alloys also reported downshifts of the d-band center. For instance, the downward shift of the d-band center of Pt−Co alloy was observed by in situ X-ray absorption spectroscopy, where the Pt−Co alloy exhibited a

significantly increased d-band vacancy compared to that of a pure Pt.[52] Meanwhile, Watanabe and co-workers showed that the upward shift of the Fermi level of Pt−Co alloy by the charge transfer from Co to Pt atoms[51,53] caused a relative downshift of the d-band center as well as the core levels with respect to the Fermi level.[49,54] In fact, Co 2p binding energies of Pt_xCo/C were blue-shifted compared to the pure Co as the Co content increased (see Figure S7 in the Supporting Information), implying the charge transfer from Co to Pt. In addition, DFT studies revealed that the d-band center of Pt−Co alloy downshifted to that of pure Pt.[44,55] On the other hand, the observed composition-dependent ORR activities were also highly correlated with the extent of lattice contraction of Pt_xCo NCs as revealed by XRD measurements, implying that both ligand and geometric effects were present and had a combined influence on the ORR activity of Pt_xCo NCs.

To elucidate the catalytic stability of Pt_xCo NCs, we performed accelerated durability tests by applying potential cycles from 0.88 to 1.08 V at a scan rate of 0.1 V s^{-1} in O_2-saturated 0.5 M H_2SO_4 solutions at room temperature. After 5,000 cycles, the ECSA of Pt_xCo NC catalysts decreased by 11, 13.5, 26.8, 22.6, 33.3, and 41.6% for the Pt_2Co/C, Pt_3Co/C, Pt_5Co/C, Pt_7Co/C, Pt_9Co/C, and Pt_c/C, respectively (Figure 4f), demonstrating that the enhanced stability of the Pt_xCo/C catalysts could also be achieved by incorporating Co into Pt.[14]

CONCLUSIONS

In this work, we present the synthesis of highly crystalline Pt-skin Pt_xCo (x = 2, 3, 5, 7, and 9) NCs with narrow shape and size distributions. Electrocatalysis experiments showed that alloying Pt with Co could significantly improve ORR activity and durability and that the ORR activity of NCs drastically depended on their compositions. Among the various catalysts, the Pt_3Co NCs exhibited the highest specific and mass activity for the ORR. The plot of the ORR activity vs the DFT-calculated E_{OB} has a typical volcano-shape, where the Pt_3Co NC locates at the peak position, demonstrating that the Pt_3Co NCs have the optimal E_{OB} to achieve the maximum ORR activity among the various catalysts. The trends of d-band shift and lattice contraction of the Pt_xCo NCs along the variation of Co composition, obtained by XPS and XRD measurements, respectively, are distinctly correlated with that of the E_{OB}.

ASSOCIATED CONTENT

Supporting Information

Additional experimental data (Figures S1−S7 and Table S1). This material is available free of charge via the Internet at http://pubs.acs.org.

AUTHOR INFORMATION

Corresponding Author

*E-mail: wooyoun@kaist.ac.kr (W.Y.K.); sangwoohan@kaist.ac.kr (S.W.H.); joontpark@kaist.ac.kr (J.T.P.).

Author Contributions

†These authors contributed equally to this work.

Notes

The authors declare no competing financial interest.

ACKNOWLEDGMENTS

This work was supported by the National Research Foundation (NRF) of Korea Grant funded by the Korean Government (2010-0001484, 2008-0062042, 2010-0029149). We thank the staffs of KBSI and KAIST for their assistance with the TEM and XPS analyses. W.Y.K. acknowledges the TJ Park Junior Faculty Fellowship.

REFERENCES

(1) Gasteiger, H. A.; Markovic, N. M. *Science* **2009**, *324*, 48−49.
(2) Yeager, E. *Electrochim. Acta* **1984**, *29*, 1527−1537.
(3) Markovic, N. M.; Schmidt, T. J.; Stamenkovic, V.; Ross, P. N. *Fuel Cells* **2001**, *1*, 105−116.
(4) Chen, W.; Kim, J.; Sun, S.; Chen, S. *J. Phys. Chem. C* **2008**, *112*, 3891−3898.
(5) Winter, M.; Brodd, R. J. *Chem. Rev.* **2004**, *104*, 4245−4269.
(6) Abraham, K. M.; Jiang, Z. *J. Electrochem. Soc.* **1996**, *143*, 1−5.
(7) Lu, Y.-C.; Xu, Z.; Gasteiger, H. A.; Chen, S.; Hamad-Schifferli, K.; Shao-Horn, Y. *J. Am. Chem. Soc.* **2010**, *132*, 12170−12171.
(8) Peng, Z.; Yang, H. *Nano Today* **2009**, *4*, 143−164.
(9) Tian, N.; Zhou, Z.-Y.; Sun, S.-G.; Ding, Y.; Wang, Z. L. *Science* **2007**, *316*, 732−735.
(10) Mallouk, T. E. *Nature* **1990**, *343*, 515−516.
(11) Steele, B. C. H.; Heinzel, A. *Nature* **2001**, *414*, 345−352.
(12) Stamenkovic, V. R.; Fowler, B.; Mun, B. S.; Wang, G.; Ross, P. N.; Lucas, C. A.; Markovic, N. M. *Science* **2007**, *315*, 493−497.
(13) Choi, S.-I.; Choi, R.; Han, S. W.; Park, J. T. *Chem. Commun.* **2010**, *46*, 4950−4952.
(14) Choi, S.-I.; Choi, R.; Han, S. W.; Park, J. T. *Chem.—Eur. J.* **2011**, *17*, 12280−12284.
(15) Wu, J.; Zhang, J.; Peng, Z.; Yang, S.; Wagner, F. T.; Yang, H. *J. Am. Chem. Soc.* **2010**, *132*, 4984−4985.
(16) Zhang, J.; Yang, H.; Fang, J.; Zou, S. *Nano Lett.* **2010**, *10*, 638−644.
(17) Kang, Y.; Murray, C. B. *J. Am. Chem. Soc.* **2010**, *132*, 7568−7569.
(18) Yano, H.; Song, J. M.; Uchida, H.; Watanabe, M. *J. Phys. Chem. C* **2008**, *112*, 8372−8380.
(19) Stamenkovic, V. R.; Mun, B. S.; Arenz, M.; Mayrhofer, K. J. J.; Lucas, C. A.; Wang, G.; Ross, P. N.; Markovic, N. M. *Nat. Mater.* **2007**, *6*, 241−247.
(20) Chen, S.; Ferreira, P. J.; Sheng, W.; Yabuuchi, N.; Allard, L. F.; Shao-Horn, Y. *J. Am. Chem. Soc.* **2008**, *130*, 13818−13819.
(21) Jayasayee, K.; Dam, V. A. T.; Verhoeven, T.; Celebi, S.; de Bruijn, F. A. *J. Phys. Chem. C* **2009**, *113*, 20371−20380.
(22) Stamenkovic, V. R.; Mun, B. S.; Mayrhofer, K. J. J.; Ross, P. N.; Markovic, N. M.; Rossmeisl, J.; Greeley, J.; Norskov, J. K. *Angew. Chem., Int. Ed.* **2006**, *45*, 2897−2901.
(23) Salgado, J. R. C.; Antolini, E.; Gonzalez, E. R. *J. Phys. Chem. B* **2004**, *108*, 17767−17774.
(24) Yang, H.; Vogel, W.; Lamy, C.; Alonso-Vante, N. *J. Phys. Chem. B* **2004**, *108*, 11024−11034.
(25) Carlton, C. E.; Chen, S.; Ferreira, P. J.; Allard, L. F.; Shao-Horn, Y. *J. Phys. Chem. Lett.* **2012**, *3*, 161−166.
(26) Strasser, P.; Koh, S.; Anniyev, T.; Greeley, J.; More, K.; Yu, C.; Liu, Z.; Kaya, S.; Nordlund, D.; Ogasawara, H.; Toney, M. F.; Nilsson, A. *Nat. Chem.* **2010**, *2*, 454−460.
(27) Chen, Y.; Liang, Z.; Yang, F.; Liu, Y.; Chen, S. *J. Phys. Chem. C* **2011**, *115*, 24073−24079.
(28) Wang, C.; Chi, M.; Li, D.; Strmcnik, D.; van der Vliet, D.; Wang, G.; Komanicky, V.; Chang, K.-C.; Paulikas, A. P.; Tripkovic, D.; Pearson, J.; More, K. L.; Markovic, N. M.; Stamenkovic, V. R. *J. Am. Chem. Soc.* **2011**, *133*, 14396−14403.
(29) Zhang, X.-B.; Yan, J.-M.; Han, S.; Shioyama, H.; Xu, Q. *J. Am. Chem. Soc.* **2009**, *131*, 2778−2779.
(30) Shao, M.; Shoemaker, K.; Peles, A.; Kaneko, K.; Protsailo, L. *J. Am. Chem. Soc.* **2010**, *132*, 9253−9255.
(31) Wang, D.; Xin, H. L.; Yu, Y.; Wang, H.; Rus, E.; Muller, D. A.; Abruna, H. D. *J. Am. Chem. Soc.* **2010**, *132*, 17664−17666.
(32) Lim, B.; Jiang, M.; Camargo, P. H. C.; Cho, E. C.; Tao, J.; Lu, X.; Zhu, Y.; Xia, Y. *Science* **2009**, *324*, 1302−1305.

(33) Sasaki, K.; Naohara, H.; Cai, Y.; Choi, Y. M.; Liu, P.; Vukmirovic, M. B.; Wang, J. X.; Adzic, R. R. *Angew. Chem., Int. Ed.* **2010**, *49*, 8602−8607.
(34) Wang, C.; van der Vliet, D.; More, K. L.; Zaluzec, N. J.; Peng, S.; Sun, S.; Daimon, H.; Wang, G.; Greeley, J.; Pearson, J.; Paulikas, A. P.; Karapetrov, G.; Strmcnik, D.; Markovic, N. M.; Stamenkovic, V. R. *Nano Lett.* **2011**, *11*, 919−926.
(35) Kim, Y.; Hong, J. W.; Lee, Y. W.; Kim, M.; Kim, D.; Yun, W. S.; Han, S. W. *Angew. Chem., Int. Ed.* **2010**, *49*, 10197−10201.
(36) Wang, J. X.; Ma, C.; Choi, Y.; Su, D.; Zhu, Y.; Liu, P.; Si, R.; Vulmirovic, M. B.; Zhang, Y.; Adzic, R. R. *J. Am. Chem. Soc.* **2011**, *133*, 13551−13557.
(37) Wang, C.; Daimon, H.; Onodera, T.; Koda, T.; Sun, S. *Angew. Chem., Int. Ed.* **2008**, *47*, 3588−3591.
(38) Bard, J.; Faulkner, L. R. *Electrochemical Methods: Fundamentals and Applications*: Wiley: New York, 2000.
(39) Kresse, G.; Hafner, J. *Phys. Rev. B* **1993**, *47*, R558−R561.
(40) Kresse, G.; Hafner, J. *Phys. Rev. B* **1994**, *49*, 14251−14269.
(41) Kresse, G.; Furthmüller, J. *Phys. Rev. B* **1996**, *54*, 11169−11186.
(42) Kresse, G.; Furthmüller, J. *Comput. Mater. Sci.* **1996**, *6*, 15−50.
(43) Perdew, J. P.; Burke, K.; Ernzerhof, M. *Phys. Rev. Lett.* **1996**, *77*, 3865−3868.
(44) Xu, Y.; Ruban, A. V.; Mavrikakis, M. *J. Am. Chem. Soc.* **2004**, *126*, 4717−4725.
(45) Moussounda, P. S.; Haroun, M. F.; Legare, P. *Phys. Scr.* **2010**, *81*, 045603(1−5).
(46) Samia, A. C. S.; Hyzer, K.; Schlueter, J. A.; Qin, C.-J.; Jiang, J. S.; Bader, S. D.; Lin, X.-M. *J. Am. Chem. Soc.* **2005**, *127*, 4126−4127.
(47) Borchert, H.; Shevchenko, E. V.; Robert, A.; Mekis, I.; Kornowski, A.; Grubel, G.; Weller, H. *Langmuir* **2005**, *21*, 1931−1936.
(48) Cordero, B.; Gomez, V.; Platero-Prats, A. E.; Reves, M.; Echeverria, J.; Cremades, E.; Barragan, F.; Alvarez, S. *Dalton Trans.* **2008**, *37*, 2832−2838.
(49) Hammer, B.; Norskov, J. K. *Nature* **1995**, *376*, 238−240.
(50) Snyder, J.; McCue, I.; Livi, K.; Erlebacher, J. *J. Am. Chem. Soc.* **2012**, *134*, 8633−8645.
(51) Wakisaka, M.; Mitsui, S.; Hirose, Y.; Kawashima, K.; Uchida, H.; Watanabe, M. *J. Phys. Chem. B* **2006**, *110*, 23489−23496.
(52) Mukerjee, S.; Srinivasan, S.; Soriaga, M. P.; McBreen, J. *J. Electrochem. Soc.* **1995**, *142*, 1409−1422.
(53) Cabeza, G. F.; Legare, P.; Castellani, N. J. *Surf. Sci.* **2000**, *465*, 286−300.
(54) Uchida, H.; Yano, H.; Wakisaka, M.; Watanabe, M. *Electrochemistry* **2011**, *79*, 303−311.
(55) Menning, C. A.; Chen, J. G. *J. Chem. Phys.* **2008**, *128*, 164703(1−9).